Soft-x-ray spectroscopy of coronene$^+$ and (coronene+H)$^+$ cations: The influence of hydrogenation on electronic structure and photofragmentation

Yining Huo,[1] Mónica K. Espinoza Cangahuala,[1] Marcelo Goulart,[1] Vicente Zamudio-Bayer,[2] Markus Kubin,[2] Martin Timm,[2] J. Tobias Lau,[2,3] Bernd von Issendorff,[3] Ronnie Hoekstra,[1,4] Shirin Faraji,[1] and Thomas Schlathölter[1,5]

[1]*Zernike Institute for Advanced Materials, University of Groningen, Nijenborgh 4, 9747AG Groningen, Netherlands*

[2]*Abteilung für Hochempfindliche Röntgenspektroskopie, Helmholtz-Zentrum Berlin für Materialien und Energie, 12489 Berlin, Germany*

[3]*Physikalisches Institut, Universität Freiburg, 79104 Freiburg, Germany*

[4]*Advanced Research Center for Nanolithography (ARCNL), Science Park 106, 1098 XG Amsterdam, Netherlands*

[5]*University College Groningen, University of Groningen, Hoendiepskade 23/24, 9718 BG Groningen, Netherlands*

(Received 27 June 2022; revised 4 October 2022; accepted 23 November 2022; published 14 December 2022)

We have studied soft-x-ray absorption in coronene and in singly hydrogenated coronene cations. Hydrogenation on the one hand closes the singly occupied molecular orbital of the coronene radical cation and thus decreases the reactivity of the molecule. On the other hand, the additional H atom breaks the coronene D_{6h} symmetry and exhibits a comparably small binding energy. The effect of single hydrogenation on soft-x-ray photoionization is therefore hard to predict. In our experiments, the mass selected polycyclic aromatic hydrocarbons' cations were stored in a cryogenic radio-frequency ion trap and exposed to monochromatic x rays with energies around the carbon *K* edge. The partial photoion yields were recorded as a function of photon energy by means of time-of-flight mass spectrometry. The experimental data was compared to time-dependent density-functional theory calculations based on a short-range corrected functional. The combination of experiment and theory allowed for precise assignment of 1*s* excitations to the resonances in the spectra. We found that these resonant transitions as well as direct 1*s* ionization into the continuum could induce nondissociative ionization, H/H_2 loss, as well as fragmentation of the carbon backbone. For multiple ionization, neutral hydrogen loss was found to compete with fission reactions where H^+ or $H_2{}^+$ is released. H attachment was found to substantially decrease backbone fragmentation.

DOI: 10.1103/PhysRevA.106.063104

I. INTRODUCTION

Polycyclic aromatic hydrocarbons (PAHs) in their neutral and ionic form are commonly thought to be abundant in numerous objects inside our galaxy and beyond. The key signature of these PAHs are the aromatic infrared bands (AIBs) that are present in the emission spectra of many astronomical objects [1,2]. In many of these environments, PAHs can exist in neutral or ionic form [3] and can be partially hydrogenated [4,5]. Also the diffuse interstellar (absorption) bands (DIBs) in the infrared, visible, and UV are commonly assigned to PAH-based species, even though at present only C_{60}^+ has been unambiguously identified as a carrier of DIB lines [6]. PAHs or syperhydrogenated PAH cations could contribute to the DIBs as well, as they are known to feature the observed transitions in the visible [7,8].

PAHs are known to have large photoabsorption cross sections in the vacuum ultraviolet (VUV). In space, VUV photons are abundant as they are for instance emitted by hot stars, which is why (dissociative) VUV photoionization of neutral PAHs and PAH cations has been intensively studied over the years. In a seminal study, Jochims *et al.* studied VUV induced dissociation of neutral PAH molecules and found that relaxation proceeds via H, H_2, and C_2H_2 loss in small PAHs of up to about 30 carbon atoms [9]. More recent research has focused on VUV absorption in PAH cations, trapped in radio-frequency (rf) ion traps. In particular, above the ionization threshold, for large systems such as $C_{42}H_{18}{}^+$ nondissociative ionization (NDI) dominates [10], with about 98% of the molecules remaining intact upon VUV absorption [11], whereas for smaller PAHs up to $C_{24}H_{12}{}^+$ ionization is accompanied by dissociation or fragmentation [12].

Hot astronomical objects with temperatures in the 10^6–10^8 K range emit (soft) x rays [13,14]. Draine has for instance modeled soft-x-ray attenuation due to carbonaceous and silica dust grains at the carbon and silicon *K* edges [15] and suggested to study dust composition by observation of bright extragalactic soft-x-ray point sources. Schneider and Schmidt have studied the carbon content of the debris disk around a young star, using absorption features in the young stars spectrum [16]. At present, the lack in high-resolution soft-x-ray reference spectra makes it difficult to conduct similar studies on PAHs [17].

A soft-x-ray based experimental technique that is sensitive to the electronic structure and in particular to the unoccupied molecular orbitals is x-ray-absorption near-edge structure (XANES), often called near-edge x-ray-absorption fine structure (NEXAFS). Only very few experimental NEXAFS studies have focused on gas-phase PAHs, yet. Fronzoni *et al.* [18] performed carbon *K*-edge NEXAFS studies on

neutral phenantrene and coronene and compared their total photoion yield data to quantum chemical calculations. Good agreement between experiment and theory was only reached when vibronic coupling was taken into account. Reitsma *et al.* investigated soft-x-ray absorption in coronene cations in a rf ion trap [19,20] using near-edge x-ray-absorption mass spectrometry (NEXAMS [21]), where partial photoion yields for various different photoproducts are recorded as a function of soft-x-ray energy. Deexcitation by sequential H loss was observed and the number of lost H atoms was found to correlate with the excitation energy of the final state of the 1*s* excitation. The energy resolution however was rather low, making an in-depth analysis of spectra features difficult.

Previous research indicated that moderate hydrogenation of coronene cations can increase the stability of the C backbone upon excitation [20,22]: vibrational energy is required to "boil off" the extra hydrogen atoms, effectively cooling the remaining molecular cation. If seven or more hydrogen atoms are added, the hydrogen-induced weakening of the molecular C backbone becomes the dominating effect and stability dramatically decreases [22]. For neutral pyrene molecules, initial collision studies showed the dominating effect of C backbone weakening upon addition of several H atoms [23,24]. A comprehensive VUV photofragmentation study recently proved that, also for (neutral) pyrene, a protective effect of hydrogenation can be observed for the case of four hydrogen atoms, whereas the addition of six hydrogen atoms already destabilizes the system [25].

In this work, we thoroughly studied the effect of single hydrogen atom attachment to coronene cations on the molecular stability. To this end, we investigated coronene radical cation ($C_{24}H_{12}{}^{+}$, cor^{+}) and hydrogenated coronene cations ($C_{24}H_{13}{}^{+}$, $[cor + H]^{+}$) by high-resolution NEXAMS. The precursor ions were accumulated in a cryogenic rf ion trap, exposed to monochromatic soft x rays and photoions were then mass analyzed by means of time-of-flight (TOF) spectrometry. Photoion yields were recorded as a function of the photon energy to study the influence of hydrogenation on the electronic structure and on the stability of the carbon skeleton for both cor^{+} and its hydrogenated counterpart. Hydrogenation of the coronene radical cation closes the singly occupied molecular orbital, thereby decreasing the reactivity of the cation. At the same time, single hydrogenation H breaks the symmetry of the molecule. The overall effect of single hydrogenation on cor^{+} stability following soft-x-ray photoabsorption is hard to predict.

To interpret the experimental data, time-dependent density-functional theory (TD-DFT) was adopted to compute the NEXAFS spectra for cor^{+} and $[cor + H]^{+}$ at the carbon *K* edge. We have employed a short-range corrected (SRC) functional that is ideally suited for the description of inner-shell excitation processes. (See Fig. 1.)

II. EXPERIMENT

All experiments were conducted using the Ion Trap apparatus [26–28], a permanent end-station at the UE52-PGM high-resolution soft-x-ray beamline at the BESSY II synchrotron facility (Helmholtz Zentrum Berlin). The ions were brought into the gas phase by means of electrospray ionization (ESI). For preparation of 1 ml of sample solution, we used 650 μl of a saturated coronene (Sigma Aldrich, $\geqslant$ 99% purity) solution in methanol, diluted with 300μl methanol. 50μl 10 mmol/L $AgNO_3$ was added to facilitate charge transfer from coronene to Ag^{+} ions in solution. $[cor + H]^{+}$ was produced by exposure of the rf-guided beam of cor^{+} ions to a thermal beam of H atoms. To produce atomic hydrogen, a 27 MHz discharge source [29] was used. The standard exit capillary was replaced by an optically blind teflon capillary system [30] which was extended for direct injection in a trap while maintaining a dissociation degree of ≈30% [31]. The cor^{+} and $[cor + H]^{+}$ cations did not react with H_2 molecules as was tested by switching the discharge source off and injecting a pure H_2 beam. The cor^{+} or $[cor + H]^{+}$ ions were then mass selected by a quadrupole mass filter and accumulated in a cryogenic ($T \approx 20$ K) linear rf ion trap. NEXAMS is an action-spectroscopy technique where the photon energy $E_{\text{x ray}}$ is ramped in small steps across the C *K* edge. For each $E_{\text{x ray}}$, the trapped PAH cations were exposed to monochromatic ($\Delta E \approx 50$ meV) soft x rays and the entire trap content including the photoproducts was extracted into a reflectron-type TOF mass spectrometer. The relative yields of the different photoions were determined as a function of the x-ray energy $E_{\text{x ray}}$.

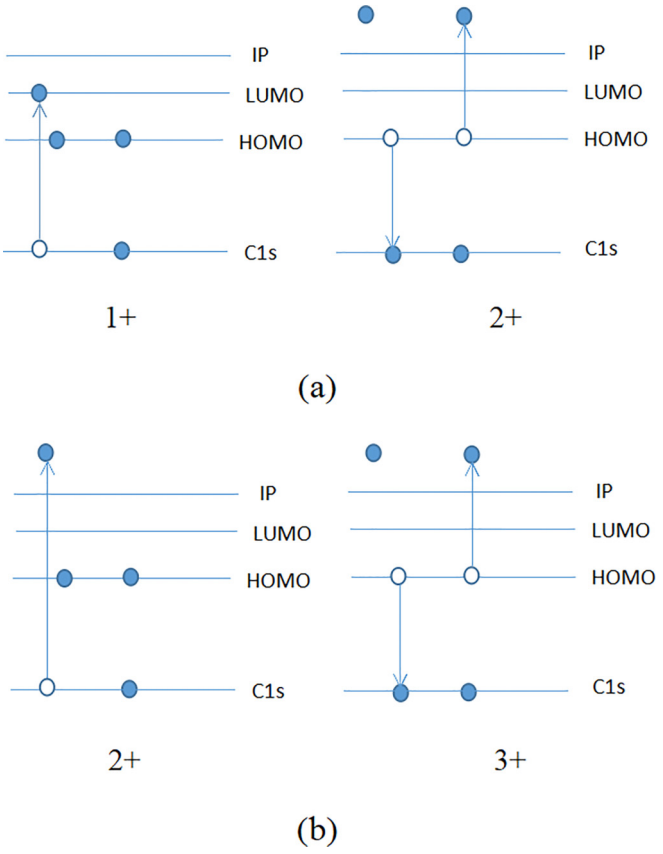

FIG. 1. Schematic representation of C *K*-shell photoabsorption processes: (a) 1*s* excitation followed by Auger decay and (b) direct 1*s* ionization followed by Auger decay.

III. THEORY

To date, a variety of techniques have been employed to compute x-ray-absorption spectra for isolated molecules such

as Stieltjes-Tchebycheff molecular orbital [32], multiple scattering [33], DFT-configuration interaction (CI) [34], or static exchange methods [35]. In this work, TD-DFT in the adiabatic approximation [36], a particularly accurate and widely used approach to computation of x-ray-absorption spectra, was employed. The ground-state geometries of the gas-phase coronene radical cation cor$^+$ and the singly hydrogenated coronene cation $[\mathrm{cor}+\mathrm{H}]^+$ were optimized by means of DFT using the long-range corrected hybrid density functional ωB97XD with a cc-pVDZ basis set. The convergence of the optimized molecular structures was confirmed by checking for imaginary frequencies in the vibrational frequency analysis at the same theory level. Subsequently, C 1*s* excitations were computed by means of TD-DFT using the Tamm-Dancoff approximation [37].

Here, we used the SRC-2-R1-D2 functional developed by Besley *et al.* [36,38]. In the SRC functional, the exchange functional is described by the Becke functional [39] and the correlation functional is based on a combination of the Lee-Yang-Parr (LYP) functional [40] and the Vosko-Wilk-Nusair (VWN) functional [41]. SRC exchange-correlation functionals were implemented in the Q-Chem 5.2.2 quantum chemistry package [42]. 1000 carbon core excited-state transitions are calculated for the cor$^+$ radical cation and $[\mathrm{cor}+\mathrm{H}]^+$ cation.

We have also determined adiabatic dissociation energies (ADE), defined as the difference in energy between the products and reactants in their optimized structures. Note that, due to the general high photoexcitation energies, we have not determined dissociation barriers or transition states that would reveal the appearance energies of the various pathways [25,43]. The molecules were optimized by DFT on the B3LYP/6-31G(d) level [44,45] in ADE calculations, using the ORCA program package [46]. A frequency analysis was conducted to rule out imaginary frequencies. The zero-point energy (ZPE) was corrected by a scaling factor 0.9806 [47] and included in the energy of the optimized molecular cation in order to compute the dissociation energies.

IV. RESULTS AND DISCUSSION

A. Photofragmentation spectra

As typical examples of soft-x-ray photoabsorption induced fragmentation spectra of cor$^+$ and $[\mathrm{cor}+\mathrm{H}]^+$ Fig. 2 shows spectra recorded at $E_{\mathrm{x\ ray}} = 300$ eV. Both spectra in Fig. 2 have been normalized to their respective total fragment-ion yields. For both precursor ions, the familiar structure of PAH fragmentation patterns is observed. Dominant groups of peaks appear at masses corresponding to singly charged $\mathrm{C}_N\mathrm{H}_l{}^+$. (Here and in the following, in singly charged cations N defines the number of carbon atoms and l defines the number of hydrogen atoms in a molecular photoion. In dications, an odd number of carbon atoms is defined at $N = 2N' + 1$ and an even number is defined as $N = 2N'$.) Groups of singly charged cationic fragments with a given N may contain contributions from doubly charged fragments $\mathrm{C}_{2N'}\mathrm{H}_l{}^{2+}$ which have overlapping m/z values.

A tentative estimation of the contributions of doubly charged $\mathrm{C}_{2N'}\mathrm{H}_l{}^{2+}$ cations to the $\mathrm{C}_N\mathrm{H}_l{}^+$ clusters of peaks might be based on intensities of the groups of peaks halfway in between the $\mathrm{C}_N\mathrm{H}_l{}^+$ groups which are solely due to doubly charged fragments with apparent half-integer values of N (i.e., dications with an odd number of C atoms, $\mathrm{C}_{2N'+1}\mathrm{H}_l{}^{2+}$), e.g., $\mathrm{C}_{13}\mathrm{H}_l{}^{2+}$ (apparent N value of 6.5) in between $\mathrm{C}_6\mathrm{H}_l{}^+$ and $\mathrm{C}_7\mathrm{H}_l{}^+$. The relative yields of doubly charged fragment cations generally increase with decreasing N. For the hydrogenated system, systematically lower yields of doubly charged fragment cations are observed.

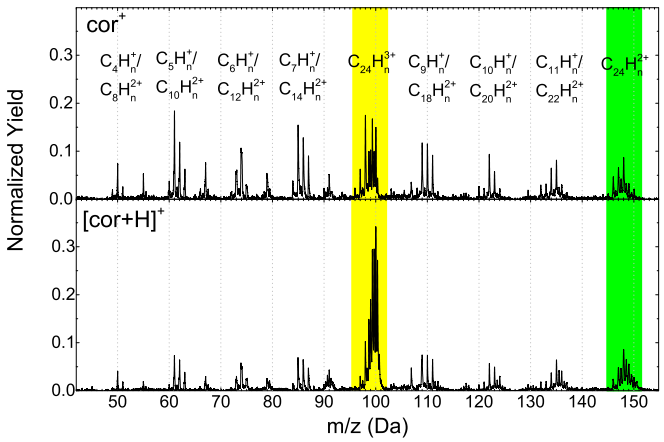

FIG. 2. Fragmentation spectra of cor$^+$ (top panel) and $[\mathrm{cor}+\mathrm{H}]^+$ (bottom panel) induced by photoionization with $E_{\mathrm{x\ ray}} = 300$ eV photons. Both spectra are normalized to the respective total fragment yields. The $\mathrm{C}_{24}\mathrm{H}_n{}^{2+}$ and $\mathrm{C}_{24}\mathrm{H}_n{}^{3+}$ fragments are marked by green and yellow background.

The groups of peaks at $m/z = 150$ and $m/z = 100$ marked with green and yellow boxes in Fig. 2 do not follow these trends. A closer inspection shows that these groups are almost entirely due to multiple H loss from cor^{2+} and cor^{3+}, respectively. They correspond to $[\mathrm{C}_{24}\mathrm{H}_{12}\text{-}n\mathrm{H}]^{q+}$ (n denotes the number of lost H and q indicates the charge state) and $[\mathrm{C}_{24}\mathrm{H}_{13}\text{-}n\mathrm{H}]^{q+}$ for nonhydrogenated and hydrogenated precursors. Here, for the dication all peaks with even n can in principle have a contribution of monocations. Note that excited PAHs often favor H_2 loss over sequential H loss [9,44,48], also leading to higher peak intensities for even n. However, sequential H loss can be favored in particular cases [49]. For the trication, only the peaks at $n = 0$ and $n = 3$ can have a contribution of monocations, but all peaks have comparable intensities. We therefore conclude that, for the cor^{2+} group and for the cor^{3+} group, monocations only play a minor role. In the following sections, we will thoroughly discuss H and H_2 loss, using NEXAMS data for these two groups of peaks.

The overall mass spectral distributions for cor$^+$ and $[\mathrm{cor}+\mathrm{H}]^+$ are very similar. The only obvious exception is the group of peaks around $m/z = 100$, to which $\mathrm{C}_8\mathrm{H}_n{}^+$, $\mathrm{C}_{16}\mathrm{H}_n{}^{2+}$, and $\mathrm{C}_{24}\mathrm{H}_n{}^{3+}$ contribute. However, very strong peaks are found around $m/z = 99.3$ and 99.6 to support major contribution from $\mathrm{C}_{24}\mathrm{H}_n{}^{3+}$. For $[\mathrm{cor}+\mathrm{H}]^+$, this $m/z = 100$ group of peaks of fragment ions exceeds the other groups in yield by a factor of 3–4, whereas for cor$^+$ it is of comparable intensity. As the spectra are taken with 300 eV photons C *K* shell photon absorption leads to direct ionization followed by

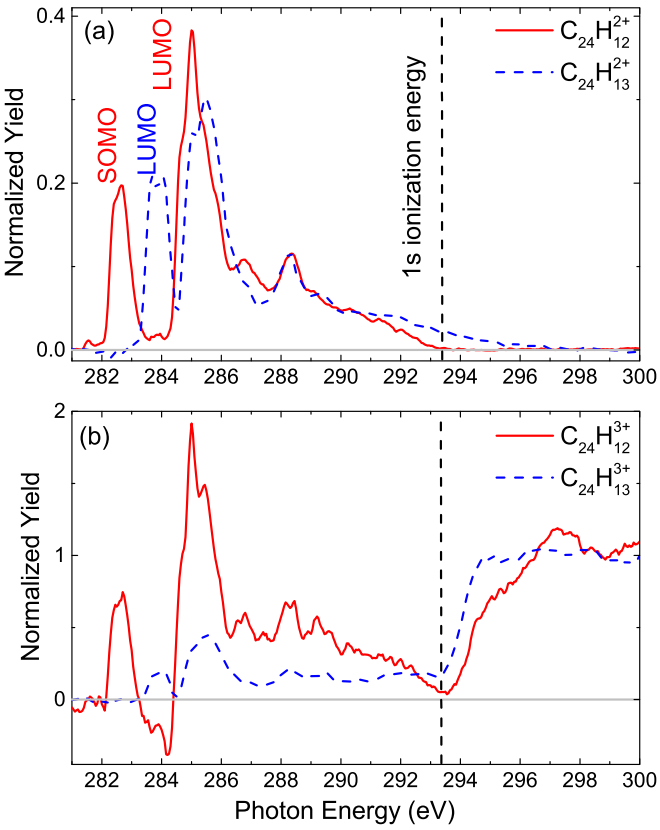

FIG. 3. Nondissociative single- (a) and double- (b) ionization NEXAMS spectra produced from either cor^+ (red solid curve) or from $[cor + H]^+$ (blue dashed curve). The vertical dashed lines indicate the approximate C 1*s* ionization energies of cor^+ and $[cor + H]^+$. Single-ionization spectra are normalized to the total yield in the excitation energy range, up to C 1*s* ionization energy. Double-ionization spectra are normalized to the near constant yield in the ionization region.

Auger decay creating an intermediate trication [see Fig. 1(b)]. It seems that these trications are more stable when starting out from $[cor + H]^+$ than from cor^+. As will be discussed in the next sections this hints at the fact that the weakly bound additional H atom which easily dissociates (over a 2.8 eV barrier) from the molecule takes away some of the internal energy of the trication, thereby enhancing its stability for the case of $[cor + H]^+$.

B. NEXAMS spectra and photon absorption calculations

Figure 3 shows the spectra for nondissociative single and double ionization of cor^+ into $C_{24}H_{12}{}^{2+}$ and $C_{24}H_{12}{}^{3+}$ and of $[cor + H]^+$ into $C_{24}H_{13}{}^{2+}$ and $C_{24}H_{13}{}^{3+}$. As discussed in detail by Reitsma *et al.* [20] for cor^+, nondissociative single ionization is predominantly the result of carbon 1*s* excitation, followed by Auger decay. The nondissociative single-ionization (NDSI) spectra in Fig. 3(a) feature a number of well-defined peaks at low $E_{x\ ray}$ that are due to resonant 1*s* excitation. For the radical cation cor^+, the lowest energy peak at about 282.5 eV is due to carbon 1*s* excitation into the singly occupied molecular orbital (SOMO). The more intense peak starting around 285 eV is due to carbon 1*s* excitation into various π^* orbitals including the lowest unoccupied molecular orbital (LUMO). Two weaker peaks show up around 287 and 288 eV. At even higher $E_{x\ ray}$, final states often have σ^* character. In this region, nondissociative single ionization of cor^+ becomes weak. For photon energies above the ionization threshold NDSI yields drop to zero as now photoabsorption leads to direct ionization and subsequent Auger decay results in double ionization. At these high photon energies, nondissociative double ionization (NDDI) is strong and only weakly dependent on photon energy [Fig. 3(b)]. The NDDI NEXAMS data in Fig. 3(b) has similar resonant features as the corresponding NDSI data, up to photon energies around 290 eV, for both cor^+ and $[cor + H]^+$. This could be due to two-electron Auger decay or due to single-electron Auger decay, where the outgoing electron induces a subsequent ionization [20,50].

The most obvious change in electronic structure that is induced by single hydrogenation of cor^+ into $[cor + H]^+$ is the fact that the SOMO fills up into the highest occupied molecular orbital (HOMO), becoming unavailable as a final state. As a consequence, the peak at 282.5 eV is absent in the NDSI data of $[cor + H]^+$ [Fig. 3(a)]. Furthermore, the cor^+ 1*s*-π^* LUMO peak at 285 eV splits up into two peaks centered at 284 eV and 285 eV. The weak peak at 287 eV is absent, whereas the peak at 288 eV is almost identical to the case of cor^+. At higher energies, nondissociative single ionization is a bit more likely for $[cor + H]^+$ than for cor^+.

At about $E_{x\ ray} \approx 293$ eV the threshold for direct carbon 1*s* ionization is reached. The 1*s* binding energy appears to be slightly lower for $[cor + H]^+$ than for cor^+. For cor^+, the transition to the ionization continuum is softer as compared to $[cor + H]^+$ where a thresholdlike increase is observed. It is interesting to note that for cor^+ the NDDI yield is smaller in the ionization continuum than at the 285 eV resonance. On the other hand, for $[cor + H]^+$ NDDI is strongest in the ionization continuum. It is very unlikely that attachment of a single H atom would lead to a dramatic change in the x-ray-photoabsorption cross section. A much more likely explanation is a higher stability of the $[cor + H]^{3+}$ trication as compared to the cor^{3+} trication.

A better understanding of the experimental NEXAMS data can be obtained by comparison to theory at the level of individual transitions. Figure 4 (top panel) displays experimental data for cor^+ photofragmentation into $C_{24}H_8{}^+$ (loss of 4 H atoms). The bottom panel shows a stick spectrum obtained by TD-DFT. The energy axes of experiment and theory are shifted by 1 eV with respect to each other to align peak positions. The resonances in the NEXAMS spectra are fitted with Gaussians, labeled CK1 to CK5. From the stick spectrum it is obvious that each peak is due to a number of different transitions. The CK1 resonance at $E_{x\ ray} \approx 282.5$ eV is due to 1*s* transitions to the SOMO [S(1)]. The inset associated to the lowest-energy transition shows an isosurface plot of the SOMO. As all partly occupied or unoccupied states in coronene, the SOMO exhibits the perfect D_{6h} symmetry of coronene. The orbital has π^* character. The second resonance in Fig. 4 (top) at $E_{x\ ray} \approx 285$ eV has a double structure and is therefore fitted by two Gaussians CK2 and CK3. As for the SOMO, the stick spectrum reveals that CK2 and CK3 are due to several transitions to the lowest unoccupied molecular

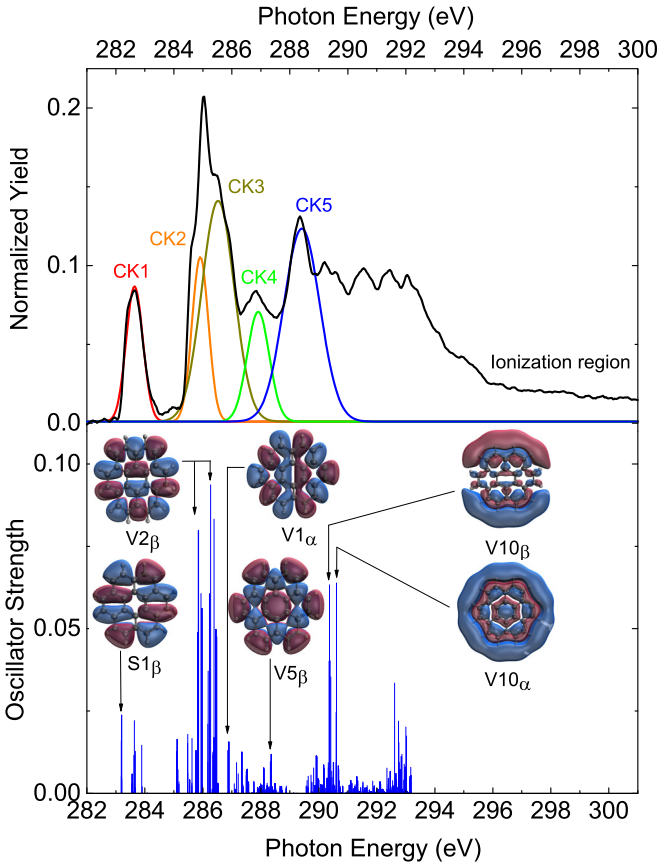

FIG. 4. Top panel: NEXAMS data for cor$^+$ photofragmentation into $C_{24}H_8^+$ with Gaussian fits to the main spectral features. Bottom panel: stick spectra of oscillator strengths for cor$^+$ excitation obtained by TD-DFT (SRC2-R1/cc-pVDZ). The insets show isosurface plots for a number of unoccupied molecular orbitals. Here and in the other figures, the labels "V" and "S" denote virtual orbitals and SOMO, respectively. The number indicates the energetic ordering of the molecular orbital. LUMO: V(1) and LUMO+1: V(2), etc. α and β represent the electron spin.

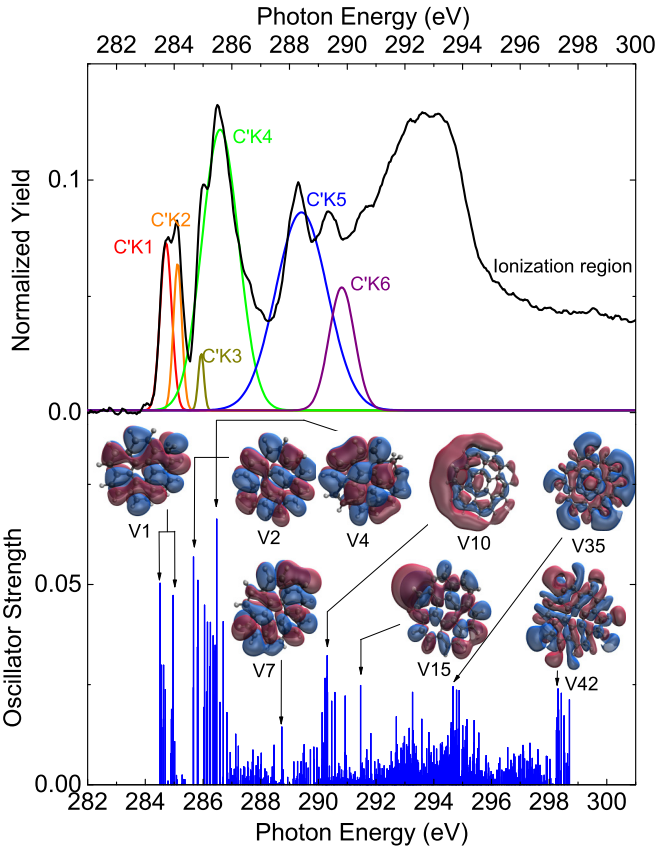

FIG. 5. Top panel: NEXAMS data for $[\mathrm{cor}+\mathrm{H}]^+$ photofragmentation into $C_{24}H_8^+$ with Gaussian fits to the main spectral features. Bottom panel: stick spectrum of oscillator strengths for $[\mathrm{cor}+\mathrm{H}]^+$ excitation obtained by TD-DFT (SRC2-R1/cc-pVDZ). The insets show isosurface plots for a number of unoccupied molecular orbitals.

orbitals. Two insets show the isosurface plots for $V(1)_\alpha$ and $V(2)_\beta$, which clearly have π^* character. Also the weaker resonances CK4 and CK5 are due to a multitude of (higher-lying) transitions. In the range from 290 eV to 295 eV, a broad plateau is observed, which is due to a mixture of π^* and σ^* states, as is obvious from the two isosurface plots for $V(10)_\alpha$ and $V(10)_\beta$.

Figure 5 shows the corresponding comparison between experiment and theory for photofragmentation of hydrogenated coronene cations $[\mathrm{cor}+\mathrm{H}]^+$ into the same fragment $C_{24}H_8^+$ (here, this fragment corresponds to loss of five H atoms, instead of four). The general differences in NEXAMS spectra between cor$^+$ and $[\mathrm{cor}+\mathrm{H}]^+$ are similar to those observed in Fig. 3 for nondissociative photoabsorption. In a nutshell, the SOMO peak vanishes and, instead, an additional low-energy peak C′K1 at 283.5 eV is observed that corresponds to 1*s*-LUMO transitions. The isosurface plot of the V1 LUMO orbital has mostly π^* character, but the D_{6h} symmetry is broken due to the added H atom. The main peak at 285 eV appears again to consist of two contributions C′K3 and C′K4, both of which are due to several transitions to low-lying unoccupied orbitals of mostly π^* character. Due to the broken symmetry, the character of the orbitals is less clear than for the case of cor$^+$, though. Two peaks in the lower part of the energy range of $E_{\mathrm{x\ ray}} \approx 288$–$299$ eV are labeled C′K5 and C′K6. The corresponding isosurface plots show a stronger contribution of σ^* character. At higher energies (290 to 295 eV) once again a broad continuum is observed that arises from a large number of individual transitions. They are labeled CK*b* for cor$^+$ and C′K*b* for $[\mathrm{cor}+\mathrm{H}]^+$. The unoccupied orbitals involved in these transitions have strong σ^* character and many of them exhibit strong asymmetries, as is clear from the isosurface plots of orbitals V(35) and V(42).

More details on the orbital structures can be found in the Supplemental Material [51].

C. H and H_2 loss processes as a function of photon energy

As can be seen from Fig. 2, soft-x-ray photoabsorption leads to a wide variety of fragment species. In particular in the 1*s excitation* regime, i.e., below the direct 1*s* ionization threshold, fragmentation depends strongly on photon energy. To further investigate this photon energy dependence for single- and double-ionization processes, we have studied H

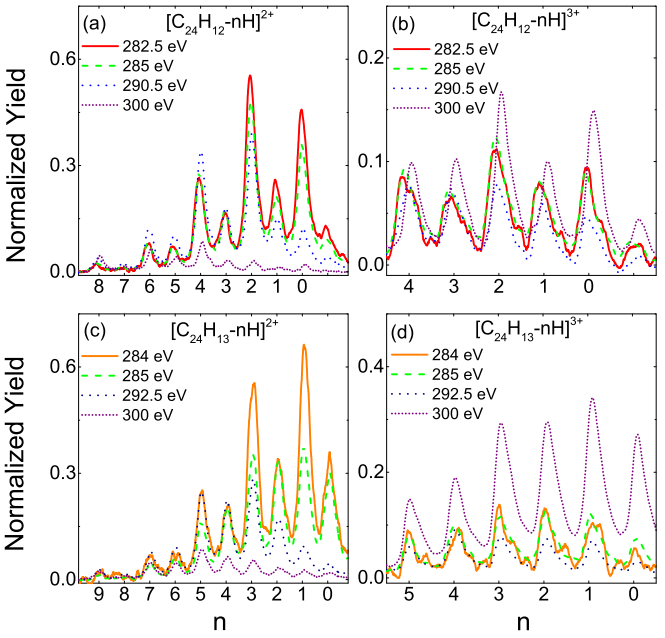

FIG. 6. $[C_{24}H_{12}\text{-}nH]^{q+}$ and $[C_{24}H_{13}\text{-}nH]^{q+}$ dicationic ($q = 2$) and tricationic ($q = 3$) mass spectra as a function of the number of lost H for four characteristic photon energies: $E_{\text{x ray}} = 282.5$ eV, 285 eV, 290.5 eV, and 300 eV for cor^+, while $E_{\text{x ray}} = 284$ eV, 285 eV, 292.5 eV, and 300 eV for $[\text{cor} + \text{H}]^+$. Top panel: cor^+. Bottom panel: $[\text{cor} + \text{H}]^+$.

and H_2 loss from cor^{2+} and cor^{3+} and from $[\text{cor} + \text{H}]^{2+}$ and $[\text{cor} + \text{H}]^{3+}$.

Figure 6 shows the mass-spectral regions that feature dications and trications for cor^+ and for $[\text{cor} + \text{H}]^+$ precursors at $E_{\text{x ray}} = 282.5$ eV (CK1), 285 eV (CK2, CK3), 288.5 eV, 290.5 eV (CK5), and 300 eV (cor^+), and $E_{\text{x ray}} = 284$ eV (C′K1, C′K2), 285 eV (C′K3, C′K4), 288.5 eV (C′K5), 292.5 eV, and 300 eV ($[\text{cor} + \text{H}]^+$). Generally, for each system the first two energies are in a range that is dominated by unoccupied orbitals with π^* character, the next two energies are in a range where unoccupied states have more σ^* character, while $E_{\text{x ray}} = 300$ eV is deep in the $1s$ ionization continuum. For a further interpretation of our data, it is important to realize that an excited $\text{cor}^{2+}/[\text{cor} + \text{H}]^{2+}$ or $\text{cor}^{3+}/[\text{cor} + \text{H}]^{3+}$ (formed by single or double ionization of the cor^+ or $[\text{cor} + \text{H}]^+$ precursor) can lead to both neutral H/H_2 loss or loss of cationic $\text{H}^+/\text{H}_2{}^+$. Paris *et al.* [52] have shown that the dissociation energy for neutral H/H_2 loss from cor^{q+} is relatively independent on the charge state q ($q = 0$–5) and amounts to 4–5 eV. The dissociation energy for cationic $\text{H}^+/\text{H}_2{}^+$ is similar only for $q = 3$. For $q \leqslant 3$ cation loss is energetically much less favorable (dissociation energies around 9–10 eV). For $q = 4$, cation loss is actually much more favorable (dissociation energies around 3 eV).

The dication data are shown in Figs. 6(a) and 6(c). Loss of up to $n = 6$ H atoms is observed for cor^+ and up to $n = 7$ H for $[\text{cor} + \text{H}]^+$. In Figs. 6(a) and 6(b), the peaks located on rightmost positions are due to isotope effects, where the ^{13}C isotopic abundance is around 26% for coronene. For cor^+ precursor ions, H loss exhibits the commonly observed oscillatory structure with even n fragments dominating [48,53].

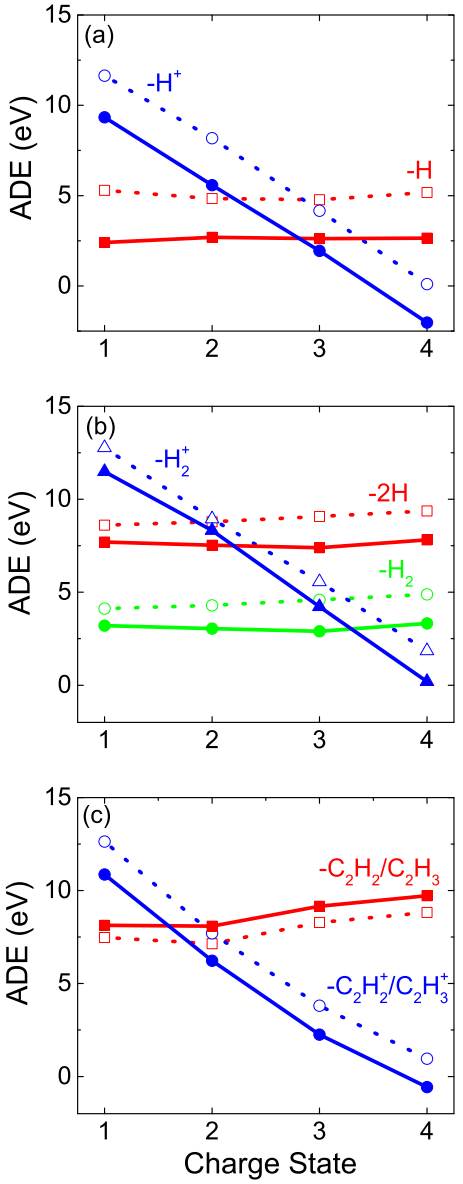

FIG. 7. Adiabatic dissociation energies (ADE) for different fragmentation channels as a function of the cationic charge state q of cor^{q+} (dashed lines) and $[\text{cor} + \text{H}]^{q+}$ (solid lines) as determined by DFT calculations on the B3LYP/6-31G(d) level. In (a), red curves: H loss; blue curves: H^+ loss. In (b), red curves: 2H loss; green curves: H_2 loss; blue curves: $\text{H}_2{}^+$ loss. In (c), red curves: $\text{C}_2\text{H}_2/\text{C}_2\text{H}_3$ loss; blue curves: $\text{C}_2\text{H}_2{}^+/\text{C}_2\text{H}_3{}^+$ loss. Details of calculation are included in the Supplemental Material.

This is in agreement with the calculations of Paris *et al.*, who find H_2 loss being favored over H loss from cor^{2+} [52]. Interestingly, for the $[\text{cor} + \text{H}]^+$ precursor, a very similar fragmentation pattern is observed for the lowest photon energy only, indicating that here the H-loss sequence is started with loss of the single extra H atom. Subsequent losses are then similar to the case of the cor^+ precursor. In $[\text{cor} + \text{H}]^+$, the oscillations are generally less pronounced.

Figure 7 shows the ADE for $C_{24}H_{12}{}^{q+}$ (cor^{q+}) as calculated in [52] and for $C_{24}H_{13}{}^{q+}$ ($[\text{cor} + \text{H}]^{q+}$), as determined by DFT on the B3LYP/6-31G(d) level. It is clear that here, for

the hydrogenated system, dissociation energies for both H and H_2 are markedly lower (≈3 eV vs ≈5 eV). In contrast to the nonhydrogenated system, for $[cor + H]^{q+}$ H loss is energetically favored over H_2 loss. The ADE for the charge separation channel, i.e., loss of either H^+ or $H_2{}^+$, follow the same trend for cor^{q+} and $[cor + H]^{q+}$. The dissociation energies for the latter are again systematically lower. The theoretical data thus clearly supports the interpretation of an initial loss of the weakly bound extra H atom from $[cor + H]^{q+}$, before the system further deexcites as cor^{q+} (but with reduced internal energy). The intersection between the dissociation energies for neutral and for charged H/H_2 is observed at $q = 3$ for both cor^{q+} and $[cor + H]^{q+}$.

How does this manifest in the spectra shown in Figs. 6(a) and 6(c)? For both precursor ions, the average number of lost H atoms is increasing with $E_{x\ ray}$. The lowest-energy resonances at 282.5 eV (cor^+) and at 284 eV ($[cor + H]^+$) are most intense at $n = 2$ and $n = 1$, respectively. For higher $E_{x\ ray}$, this shifts to $n = 4$ and $n = 3$, respectively, with the exception of $E_{x\ ray} = 300$ eV. Here, maximum fragment yields are observed for $n = 4$ and $n = 5$, respectively, with very small yields for lower n. Very likely, in both systems the high n fragments stem from an intermediate trication, where neutral and cationic H_2 loss competes. The trication shrinks by neutral H_2 emission and Coulomb repulsion increases so that cationic loss of H^+ or $H_2{}^+$ will be favored for higher n.

For the trication data [Figs. 6(b) and 6(d)] at the two low-energy resonances oscillations are generally weaker (cor^+) or absent ($[cor + H]^+$) as compared to the dication data in panels (a) and (c). Strongest yields are obviously observed for $E_{x\ ray} = 300$ eV, deep in the ionization continuum, as double electron removal into an (intermediate) trication is expected to be the dominant process. For the $[cor + H]^+$ precursor, at this energy the yields are about a factor of 3 larger than for all energies in the excitation regime. For the cor^+ precursor, the difference in yield between ionization at 300 eV and excitation at lower energies is much less.

At 300 eV, H losses peak at $n = 2$ (cor^+) and $n = 1$ ($[cor + H]^+$), which is complementary to what is observed in the dicationic system, where much higher n are observed. This completes the charge separation picture drawn above: the transient trications are first subject to loss of one or few neutral H or H_2 units and the corresponding ions can be observed as cations. With increasing n Coulomb repulsion increases and so does the probability for H^+ or $H_2{}^+$ loss, so that the systems shift to the dicationic series.

It is interesting to note that, for lower photon energies, trends are similar to what is observed for the dicationic species. H loss peaks at $n = 2$ for the lowest resonances. These values shift to $n = 4$ and $n = 5$ for $E_{x\ ray} = 290$ eV and 292.5 eV in cor^+ and $[cor + H]^+$, respectively. We attribute the formation of these trications to Auger double ionization, i.e., emission of two valence electrons in the decay of the initial 1s vacancy [54,55].

Figure 8 now displays the NEXAMS data of the different H loss channels for both dications and trications, including the spectra for $n = 0$ already presented in Fig. 3. In order to quantify NEXAMS spectral evolution as a function of H/H_2 loss, the spectra are labeled by their respective n. The dication spectra for both precursors show qualitatively similar trends: the two low-energy resonances dominate for $n = 0$ and decrease in relative intensity when n is increasing. In parallel, the broadband observed for both precursors at higher excitation shows a strong blueshift with increasing n and also strongly increases in relative intensity. As expected, higher excitation energies correspond to an increase in H loss. These energies correspond to $1s \rightarrow \sigma^*$ (CH) excitations, leading to effective cleavage of the hydrogen bonds. For the $[cor + H]^+$ precursor, the high excitation energy band reaches significantly higher relative intensities.

The other striking features of the dication data in Figs. 8(a) and 8(c) are the spectral similarity of certain pairs of loss channels: for the cor^+ precursor, $n = 1$ ($C_{24}H_{11}{}^+$)and $n = 2$ ($C_{24}H_{10}{}^+$) are almost identical. Paris *et al.* have theoretically determined the barriers for dissociation pathways of coronene dications [52] and found $E_H^{cor^{2+}} = 5.2$ eV, $E_{H_2}^{cor^{2+}} = 4.95$ eV, and $E_{H+H}^{cor^{2+}} = 8.7$ eV (the H_2 and H+H barriers are for H atoms attached to neighboring C atoms). The very similar dissociation barriers for H loss and H_2 loss are in line with the almost identical NEXAMS data for these channels. Figure 8 shows that also the subsequent H or H_2 losses are paired: $n = 3$ ($C_{24}H_9{}^+$) and $n = 4$ ($C_{24}H_8{}^+$) are almost identical and so are $n = 5$ ($C_{24}H_7{}^+$) and $n = 6$ ($C_{24}H_6{}^+$)—a strong indication for a scenario in which always both H atoms attached to neighboring C atoms are eliminated, before the next ring is tackled. H loss can then be described by sequences of either H_2 loss or sequential H loss starting from an even number of H atoms l:

$$C_{24}H_l{}^{2+} \rightarrow C_{24}H_{l-1}{}^{2+} + H \rightarrow C_{24}H_{l-2}{}^{2+} + H + H,$$
$$C_{24}H_l{}^{2+} \rightarrow C_{24}H_{l-2}{}^{2+} + H_2.$$

For the $[cor + H]^+$ precursor, the dication data in Fig. 8(c) indicates that loss of the (single) extra H atom is associated to a rather low dissociation barrier: the NEXAMS data for $n = 0$ and $= 1$ are very similar. Cazaux *et al.* have determined the binding energy of the attached H atom as 2.81 eV with a negligible *attachment* barrier of only 0.01 eV [56]. The dissociation barrier is therefore about $E_{H_2}^{[cor+H]^{2+}} = 2.8$ eV, which indeed is only about half of $E_H^{cor^{2+}} = 5.2$ eV. Once the extra H atom is lost, further H loss will very likely proceed along the same pathways as for the cor^+ precursor, as precisely the same pairs of NEXAMS data are observed for cor^+ and $[cor + H]^+$.

Last but not least, above the 1s ionization threshold for both precursors the dications with multiple H losses dominate in the mass spectra. As discussed before, this part of the spectrum is most likely stemming from transient trications that lost an H^+ or an $H_2{}^+$ ion.

As discussed previously, the trication data in Figs. 8(b) and 8(d) not only show the ionization continuum but also pronounced resonant features in the excitation energy regime, which are very similar to those observed for the dication series and which are of comparable relative strength. For both cor^+ and $[cor + H]^+$ precursors, the relative intensity of the resonant features with respect to the ionization continuum increases with the number of lost H atoms. It is likely that this increase merely reflects the fact that, for the trication, H loss and H^+ loss compete and, for larger number of lost H atoms n, H^+ loss into a dication becomes more likely,

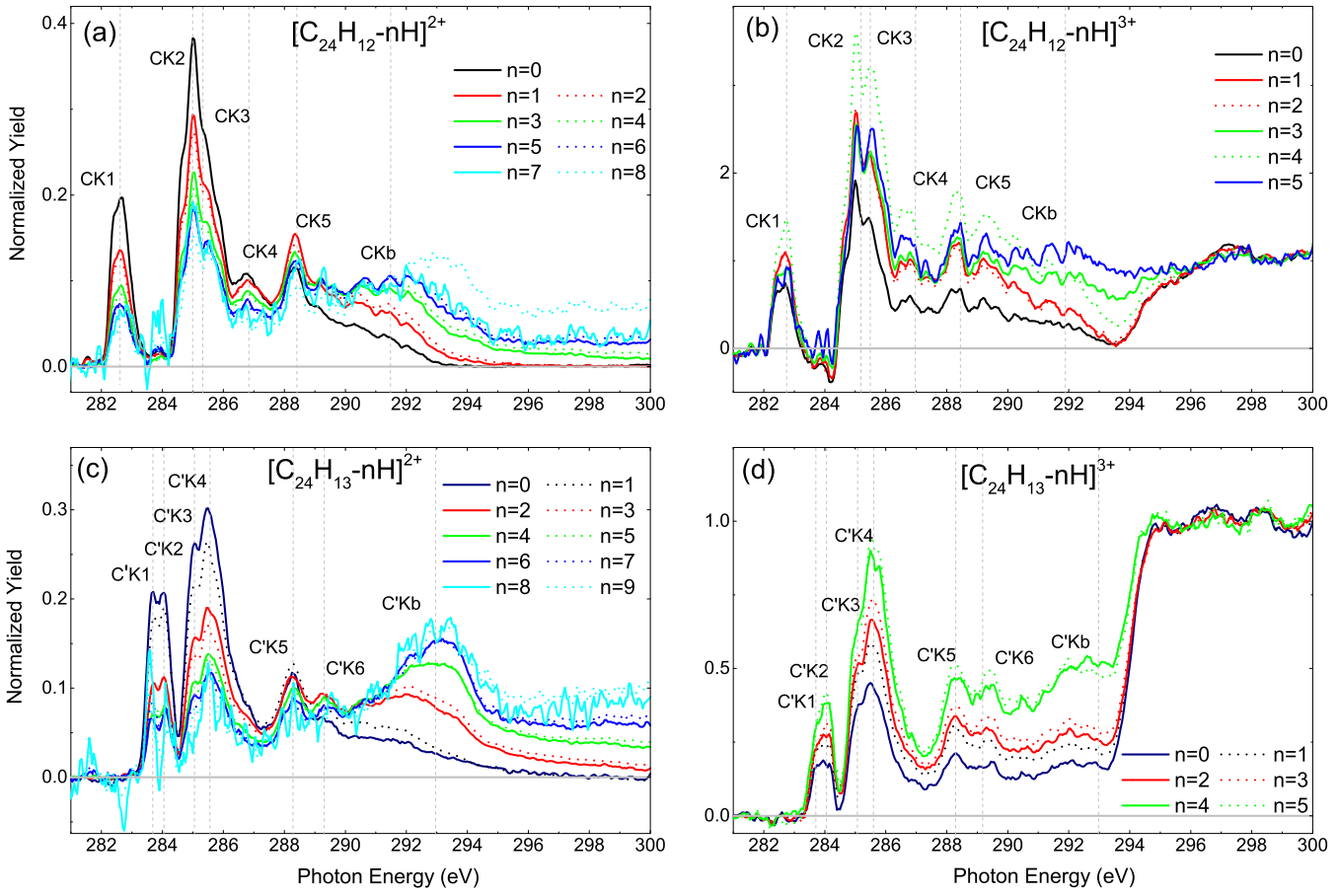

FIG. 8. NEXAMS data for $C_{24}H_{12-n}{}^{2+}$ and $C_{24}H_{12-n}{}^{3+}$ formed from cor^+ precursors (a),(b) and for $C_{24}H_{13-n}{}^{2+}$ and $C_{24}H_{13-n}{}^{3+}$ formed from $[cor + H]^+$ precursors (c),(d). Dication spectra are normalized to the integral of the excitation region; trication spectra are normalized to the yields in the ionization continuum.

depleting the corresponding trication peak. From the data it is clear that relatively more trications are formed from $[cor + H]^+$ precursors, indicating a stabilization due to H attachment.

D. H/H_2 loss yields

To get a deeper insight into the photon energy dependence of the NEXAMS spectra, Fig. 9 displays the relative contribution of the different peaks as a function of the number of lost H atoms for dication formation from cor^+ (left) and $[cor + H]^+$ (right).

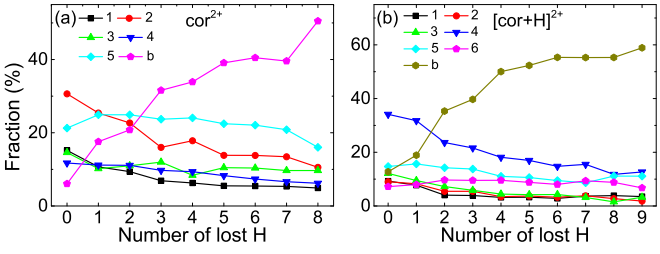

FIG. 9. Relative contribution of the individual peaks CKp (p = 1–5 or $p = b$, from cor^+ precursors, left panel) and C′Kp (p = 1–6 or $p = b$, $[cor + H]^+$, right panel) from Figs. 8(a) and 8(c) as a function of lost H atoms n.

The trends observed for dications from cor^+ underline the strong dependence of H loss on excitation energy. The 1s-SOMO (CK1) and the 1s-π^* (sum of CK2 and CK3) transitions decrease strongly with n. A weaker decrease is observed for the transitions to higher-lying orbitals (CK4, CK5). The broad feature at 292 eV (CKb) follows an opposite trend and increases strongly with n. Apparently, the excitation energy of the final state of the x-ray induced carbon 1s transition can be directly related to H loss. As discussed above, it is intuitively clear that higher excitation energy enables the loss of more H atoms, but the effect is stronger than expected.

What is the effect of H attachment on soft-x-ray induced H loss? The trends observed for dications from $[cor + H]^+$ precursors qualitatively resemble those observed for cor^+. However, the decrease of the low-energy peaks with n is more pronounced, as is the increase of the broad high excitation energy feature. For instance, whereas for cor^+, the CKb yield increases almost linearly with the number of detached H atoms, for $[cor + H]^+$ the C′Kb increase is very steep for the first four H atoms before the yield saturates. In a nutshell, higher excitation is correlated with loss of more H atoms and this effect is clearly stronger for $[cor + H]^+$.

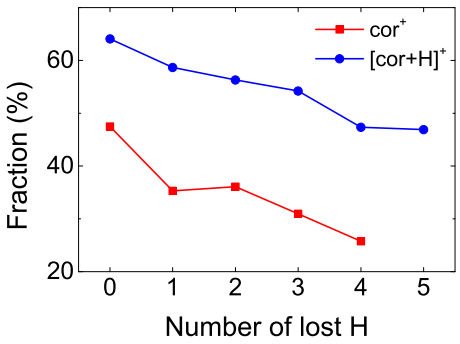

FIG. 10. Relative contribution of the ionization continuum as a function of the number of H atoms lost. Red: trication formation from cor$^+$ [from Fig. 8(b)]; blue: trication formation from $[\mathrm{cor}+\mathrm{H}]^+$ [from Fig. 8(d)].

Figure 10 now displays the relative contribution of the ionization continuum as a function of the number of lost H atoms from cor$^+$ and $[\mathrm{cor}+\mathrm{H}]^+$. For both cor$^+$ and $[\mathrm{cor}+\mathrm{H}]^+$ an almost linear decrease with n is observed with systematically larger values for $[\mathrm{cor}+\mathrm{H}]^+$.

E. Photoinduced C loss (backbone destruction)

Up to now we have focused on NDI and photoinduced H/H_2 loss. A glance at Fig. 2 (top panel) shows that $\mathrm{C}_{24}\mathrm{H}_{12-n}{}^{2+}$ ($m/z \approx 150$) and $\mathrm{C}_{24}\mathrm{H}_{12-n}{}^{3+}$ ($m/z \approx 100$) are not the only photoionization products observed for cor$^+$ precursors and the same is true for the $[\mathrm{cor}+\mathrm{H}]^+$ precursor. Instead, mostly cationic but also dicationic fragments of the type $\mathrm{C}_N\mathrm{H}_l{}^{q+}$ are observed.

To directly relate the yield for C loss to the yields for NDI and the yield of H/H_2 loss, it is useful to normalize to the total photoion yield $I_{\mathrm{total}} = I_{\mathrm{NDI}} + I_{\mathrm{H\ loss}} + I_{\mathrm{C\ loss}}$, with I_{NDI} being the total yield of ions due to ionization without any dissociation processes, $I_{\mathrm{H\ loss}}$ being the total yield of all peaks, solely due to H/H_2 loss, and $I_{\mathrm{C\ loss}}$ being the total yield of all peaks due to C loss, i.e., fragments that lack one or more C atoms.

Figure 11 shows the partial ion yields (PIY) for H loss $\frac{I_{\mathrm{H\ loss}}}{I_{\mathrm{total}}}$, for C loss $\frac{I_{\mathrm{C\ loss}}}{I_{\mathrm{total}}}$, and for NDI process $\frac{I_{\mathrm{NDI}}}{I_{\mathrm{total}}}$ as a function of photon energy in percent. A number of interesting trends

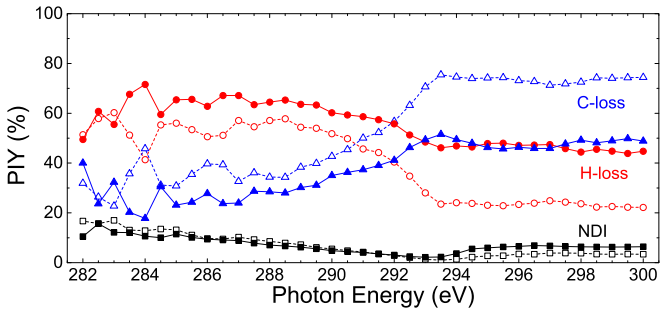

FIG. 11. Partial ion yields (PIY) of NDI (black color), PIY of fragments produced by H loss (red color), and PIY of fragments produced by C loss (blue color) as a function of photon energy for cor$^+$ precursors (dash curves) and for $[\mathrm{cor}+\mathrm{H}]^+$ precursors (solid curves).

are obvious. For the cor$^+$ precursor, highest H loss (≈60%) and lowest C loss (≈20%) is observed for 283 eV. For the remaining *excitation* regime up to about 291 eV, a plateau is observed with H loss and C loss both around 50%. Between 292 eV and 294 eV, both yields strongly change to reach their ionization plateaus of almost 75% (C loss) and a bit more than 20% (H loss). The transition from inner-shell excitation to inner-shell ionization thus leads to a marked increase in backbone fragmentation.

Hydrogenation changes the photon energy dependence quantitatively, but not qualitatively: For $[\mathrm{cor}+\mathrm{H}]^+$ maximum H loss (≈70%) and minimum C loss (≈20%) is observed at 284 eV. In the remaining excitation regime, C loss increases to about 30% and H loss decreases to about 60%. In the ionization continuum, both yields exhibit plateaus again, with H loss around 45% and C loss around 50%.

Clearly, for both cor$^+$ and $[\mathrm{cor}+\mathrm{H}]^+$, $1s$ ionization strongly increases backbone fragmentation, but this effect is weaker in $[\mathrm{cor}+\mathrm{H}]^+$. Single hydrogenation has a protective effect on the coronene C backbone.

As for H/H_2 loss, also for C loss the possibility of charge separation, i.e., loss of ionic fragments, is possible. Acetylene ($\mathrm{C}_2\mathrm{H}_2$) loss is the lowest-energy C loss channel and has often been investigated both experimentally and theoretically [9,44,48,53,57]. Figure 7(c) shows the ADE for $\mathrm{C}_2\mathrm{H}_2$ and $\mathrm{C}_2\mathrm{H}_2{}^+$ loss from cor^{q+} and for $\mathrm{C}_2\mathrm{H}_3$ and $\mathrm{C}_2\mathrm{H}_3{}^+$ loss from $[\mathrm{cor}+\mathrm{H}]^{q+}$. As already shown by Holm *et al.*, $\mathrm{C}_2\mathrm{H}_2{}^+$ loss from cor^{q+} becomes energetically competitive for $q \geqslant 2$ [44]. Essentially the same trend is observed for $\mathrm{C}_2\mathrm{H}_3{}^+$ loss from $[\mathrm{cor}+\mathrm{H}]^{q+}$. It is interesting though that dissociation energies for neutral loss are higher in the hydrogenated systems, whereas for the charge separation channel lower dissociation energies are found for $[\mathrm{cor}+\mathrm{H}]^{q+}$. For $q = 4$ and $[\mathrm{cor}+\mathrm{H}]^{q+}$, the fission energy approaches zero, i.e., the molecular ion becomes inherently unstable.

V. CONCLUSION

We have studied soft-x-ray photoionization of cor$^+$ and $[\mathrm{cor}+\mathrm{H}]^+$ cations at the C K edge in a cryogenic ion trap. The experimental data was compared to TD-DFT calculations using a SRC functional. Resonant features could directly be assigned to different classes of $1s$ excitations such as $1s$-π^* and $1s$-σ^* transitions.

NDI, H/H_2 loss as well as C loss (backbone fission) were found to be competing over the entire carbon K edge. For both precursor ions, at the lowest resonant excitation energies (multiple) H or H_2 loss is dominating the mass spectra while backbone scission (C loss) is weak. At higher excitation energies, backbone scission increases and H/H_2 loss decreases. This trend is amplified when the $1s$ ionization threshold is reached. NDI is the lowest resonant excitation energies and almost zero just below the $1s$ ionization threshold. In the ionization continuum, the yield is slightly higher again.

$[\mathrm{cor}+\mathrm{H}]^+$ systematically exhibits substantially decreased backbone scission cross sections, despite the fact that the molecular symmetry is strongly perturbed. The protective effect of the additional H can partly be attributed to the fact that excitation energy is required to "boil off" this extra atom, but there might be other contributions.

A deeper investigation of the competition between neutral H/H_2 loss and $H^+/H_2{}^+$ loss confirms earlier theoretical predictions of a transition between both fragmentation channels for the triply charged coronene cation [52].

ACKNOWLEDGMENTS

We thank HZB for the allocation of synchrotron radiation beamtime. The research leading to this result has been supported by the project CALIPSOplus under the Grant Agreement No. 730872 from the EU Framework Programme for Research and Innovation HORIZON 2020. Y.H. acknowledges support by the Chinese Scholarship Council (CSC). S.F. thanks Innovational Research Incentives Scheme Vidi 2017 with Project No. 016.Vidi.189.044, which is financed by the Dutch Research Council (NWO). The COFUND project oLife has received funding from the European Union's Horizon 2020 research and innovation programme under Grant Agreement No. 847675. The authors would like to acknowledge the contribution of the EU COST action MD-GAS (CA18212). The endstation at UE52-PGM is partially supported by BMBF Grant No. 05K16VF1. The authors thank the Center for Information Technology of the University of Groningen that provides us with the Peregrine high performance computing cluster. The authors acknowledge Dr. R. Havenith and Dr. T. L. C. Jansen for their helpful discussions.

[1] A. G. G. M. Tielens, Annu. Rev. Astron. Astrophys. **46**, 289 (2008).
[2] H. Zettergren, A. Domaracka, T. Schlathölter, P. Bolognesi, S. Díaz-Tendero, M. Łabuda, S. Tosic, S. Maclot, P. Johnsson, A. Steber, D. Tikhonov, M. C. Castrovilli, L. Avaldi, S. Bari, A. R. Milosavljević, A. Palacios, S. Faraji, D. G. Piekarski, P. Rousseau, D. Ascenzi, *et al.*, Eur. Phys. J. D **75**, 152 (2021).
[3] J. Oomens, B. G. Sartakov, A. G. G. M. Tielens, G. Meijer, and G. von Helden, Astrophys. J. Lett. **560**, L99 (2001).
[4] W. Schutte, A. Tielens, and L. Allamandola, Astrophys. J. **415**, 397 (1993).
[5] M. Bernstein, S. Sandford, and L. Allamandola, Astrophys. J. **472**, L127 (1996).
[6] E. K. Campbell, M. Holz, D. Gerlich, and J. P. Maier, Nature (London) **523**, 322 (2015).
[7] T. P. Snow, V. Le Page, Y. Keheyan, and V. M. Bierbaum, Nature (London) **391**, 259 (1998).
[8] M. Hammonds, A. Pathak, and P. Sarre, Phys. Chem. Chem. Phys. **11**, 4458 (2009).
[9] H. H. Jochims, E. Rühl, H. Baumgärtel, S. Tobita, and S. Leach, Astrophys. J. **420**, 307 (1994).
[10] J. F. Zhen, R. Castellanos, D. M. Paardekooper, N. Ligterink, H. Linnartz, L. Nahon, C. Joblin, and A. Tielens, Astrophys. J. **804**, L7 (2015).
[11] G. Wenzel, C. Joblin, A. Giuliani, S. R. Castillo, G. Mulas, M. Ji, H. Sabbah, S. Quiroga, D. Pena, and L. Nahon, Astron. Astrophys. **641**, A98 (2020).
[12] J. F. Zhen, S. R. Castillo, C. Joblin, G. Mulas, H. Sabbah, A. Giuliani, L. Nahon, S. Martin, J. P. Champeaux, and P. M. Mayer, Astrophys. J. **822**, 113 (2016).
[13] J. A. Combi, J. F. Albacete-Colombo, and J. Martí, Astron. Astrophys. **488**, L25 (2008).
[14] I. Ruffa, C. Vignali, A. Mignano, R. Paladino, and K. Iwasawa, Astron. Astrophys. **616**, A127 (2018).
[15] B. Draine, Astrophys. J. **598**, 1026 (2003).
[16] P. C. Schneider and J. H. M. M. Schmitt, Astron. Astrophys. **516**, A8 (2010).
[17] E. Costantini, S. T. Zeegers, D. Rogantini, C. P. de Vries, A. G. G. M. Tielens, and L. B. F. M. Waters, Astron. Astrophys. **629**, A78 (2019).
[18] G. Fronzoni, O. Baseggio, M. Stener, W. Hua, G. Tian, Y. Luo, B. Apicella, M. Alfé, M. de Simone, A. Kivimäki, and M. Coreno, J. Chem. Phys. **141**, 044313 (2014).
[19] G. Reitsma, L. Boschman, M. J. Deuzeman, O. Gonzalez-Magana, S. Hoekstra, S. Cazaux, R. Hoekstra, and T. Schlathölter, Phys. Rev. Lett. **113**, 053002 (2014).
[20] G. Reitsma, L. Boschman, M. J. Deuzeman, S. Hoekstra, R. Hoekstra, and T. Schlathölter, J. Chem. Phys. **142**, 024308 (2015).
[21] O. González-Magaña, G. Reitsma, M. Tiemens, L. Boschman, R. Hoekstra, and T. Schlathölter, J. Phys. Chem. A **116**, 10745 (2012).
[22] S. Cazaux, Y. Arribard, D. Egorov, J. Palotas, R. Hoekstra, G. Berden, J. Oomens, and T. Schlathölter, Astrophys. J. **875**, 27 (2019).
[23] M. Gatchell, M. H. Stockett, N. de Ruette, T. Chen, L. Giacomozzi, R. F. Nascimento, M. Wolf, E. K. Anderson, R. Delaunay, V. Vizcaino, P. Rousseau, L. Adoui, B. A. Huber, H. T. Schmidt, H. Zettergren, and H. Cederquist, Phys. Rev. A **92**, 050702(R) (2015).
[24] M. Wolf, L. Giacomozzi, M. Gatchell, N. de Ruette, M. H. Stockett, H. T. Schmidt, H. Cederquist, and H. Zettergren, Eur. Phys. J. D **70**, 85 (2016).
[25] M. H. Stockett, L. Avaldi, P. Bolognesi, J. N. Bull, L. Carlini, E. Carrascosa, J. Chiarinelli, R. Richter, and H. Zettergren, Astrophys. J. **913**, 46 (2021).
[26] K. Hirsch, J. Lau, P. Klar, A. Langenberg, J. Probst, J. Rittmann, M. Vogel, V. Zamudio-Bayer, T. Möller, and B. Von Issendorff, J. Phys. B: At., Mol., Opt. Phys. **42**, 154029 (2009).
[27] M. Niemeyer, K. Hirsch, V. Zamudio-Bayer, A. Langenberg, M. Vogel, M. Kossick, C. Ebrecht, K. Egashira, A. Terasaki, T. Möller, *et al.*, Phys. Rev. Lett. **108**, 057201 (2012).
[28] A. Langenberg, K. Hirsch, A. Ławicki, V. Zamudio-Bayer, M. Niemeyer, P. Chmiela, B. Langbehn, A. Terasaki, B. v. Issendorff, and J. T. Lau, Phys. Rev. B **90**, 184420 (2014).
[29] R. Hoekstra, A. R. Schlatmann, F. J. de Heer, and R. Morgenstern, J. Phys. B: At., Mol., Opt. Phys. **22**, L603 (1989).
[30] F. W. Bliek, G. R. Woestenenk, R. Hoekstra, and R. Morgenstern, Phys. Rev. A **57**, 221 (1998).
[31] L. Boschman, G. Reitsma, S. Cazaux, T. Schlathölter, R. Hoekstra, M. Spaans, and O. González-Magaña, Astrophys. J. **761**, L33 (2012).
[32] M. R. Hermann and P. W. Langhoff, J. Math. Phys. **24**, 541 (1983).
[33] S. I. Zabinsky, J. J. Rehr, A. Ankudinov, R. C. Albers, and M. J. Eller, Phys. Rev. B **52**, 2995 (1995).

[34] H. Ikeno and I. Tanaka, Phys. Rev. B **77**, 075127 (2008).
[35] Y. Zhang, J. D. Biggs, D. Healion, N. Govind, and S. Mukamel, J. Chem. Phys. **137**, 194306 (2012).
[36] N. A. Besley, M. J. Peach, and D. J. Tozer, Phys. Chem. Chem. Phys. **11**, 10350 (2009).
[37] S. Hirata and M. Head-Gordon, Chem. Phys. Lett. **314**, 291 (1999).
[38] N. A. Besley and F. A. Asmuruf, Phys. Chem. Chem. Phys. **12**, 12024 (2010).
[39] A. D. Becke, Phys. Rev. A **38**, 3098 (1988).
[40] C. Lee, W. Yang, and R. G. Parr, Phys. Rev. B **37**, 785 (1988).
[41] S. H. Vosko, L. Wilk, and M. Nusair, Can. J. Phys. **58**, 1200 (1980).
[42] E. Epifanovsky, A. T. B. Gilbert, X. Feng, J. Lee, Y. Mao, N. Mardirossian, P. Pokhilko, A. F. White, M. P. Coons, A. L. Dempwolff, Z. Gan, D. Hait, P. R. Horn, L. D. Jacobson, I. Kaliman, J. Kussmann, A. W. Lange, K. U. Lao, D. S. Levine, J. Liu, *et al.*, J. Chem. Phys. **155**, 084801 (2021).
[43] P. Castellanos, A. Candian, J. Zhen, H. Linnartz, and A. G. G. M. Tielens, Astron. Astrophys. **616**, A166 (2018).
[44] A. I. S. Holm, H. A. B. Johansson, H. Cederquist, and H. Zettergren, J. Chem. Phys. **134**, 044301 (2011).
[45] A. D. Becke, J. Chem. Phys. **98**, 1372 (1993).
[46] S. Lehtola, C. Steigemann, M. J. Oliveira, and M. A. Marques, SoftwareX **7**, 1 (2018).
[47] A. P. Scott and L. Radom, J. Phys. Chem. **100**, 16502 (1996).
[48] A. Ławicki, A. I. S. Holm, P. Rousseau, M. Capron, R. Maisonny, S. Maclot, F. Seitz, H. A. B. Johansson, S. Rosén, H. T. Schmidt, H. Zettergren, B. Manil, L. Adoui, H. Cederquist, and B. A. Huber, Phys. Rev. A **83**, 022704 (2011).
[49] B. West, F. Useli-Bacchitta, H. Sabbah, V. Blanchet, A. Bodi, P. M. Mayer, and C. Joblin, J. Phys. Chem. A **118**, 7824 (2014).
[50] S. Bari, D. Egorov, T. L. C. Jansen, R. Boll, R. Hoekstra, S. Techert, V. Zamudio-Bayer, C. Buelow, R. Lindblad, G. Leistner, A. Lawicki, K. Hirsch, P. S. Miedema, B. von Issendorff, J. T. Lau, and T. Schlathölter, Chem. Eur. J. **24**, 7631 (2018).
[51] See Supplemental Material at http://link.aps.org/supplemental/10.1103/PhysRevA.106.063104 for theoretical data for optimized molecular structures, molecular orbitals and total energies of molecular fragments.
[52] C. Paris, M. Alcamí, F. Martín, and S. Díaz-Tendero, J. Chem. Phys. **140**, 204307 (2014).
[53] X. Wang, H. Becker, A. C. Hopkinson, R. E. March, L. T. Scott, and D. K. Böhme, Int. J. Mass Spectrom. Ion Process. **161**, 69 (1997).
[54] A. H. Roos, J. H. D. Eland, J. Andersson, S. Zagorodskikh, R. Singh, R. J. Squibb, and R. Feifel, Phys. Chem. Chem. Phys. **18**, 25705 (2016).
[55] A. H. Roos, J. H. D. Eland, J. Andersson, R. J. Squibb, D. Koulentianos, O. Talaee, and R. Feifel, Sci. Rep. **8**, 16405 (2016).
[56] S. Cazaux, L. Boschman, N. Rougeau, G. Reitsma, R. Hoekstra, D. Teillet-Billy, S. Morisset, M. Spaans, and T. Schlathölter, Sci. Rep. **6**, 19835 (2016).
[57] J. W. L. Lee, D. S. Tikhonov, P. Chopra, S. Maclot, A. L. Steber, S. Gruet, F. Allum, R. Boll, X. Cheng, S. Düsterer, B. Erk, D. Garg, L. He, D. Heathcote, M. Johny, M. M. Kazemi, H. Köckert, J. Lahl, A. K. Lemmens, D. Loru, *et al.*, Nat. Commun. **12**, 6107 (2021).